Local structure of Sn implanted in thin SiO_2 films

S. Spiga, R. Mantovan, and M. Fanciulli
Laboratorio MDM-INFM, via C. Olivetti 2, Agrate Brianza I-20041, Italy

N. Ferretti and F. Boscherini
INFM and Department of Physics, University of Bologna, Bologna, Italy

F. d'Acapito
INFM-OGG c/o ESRF, GILDA CRG, Boîte Postale 220, F-38043, Grenoble, France

B. Schmidt, R. Grötzschel, and A. Mücklich
FZR, Institute of Ion Beam Physics and Material Research, D-01314 Dresden, Germany
(Received 26 May 2003; published 20 November 2003)

The formation and the structural properties of Sn nanocrystals produced by ion implantation in thin SiO_2 films was investigated by ^{119}Sn conversion electron Mössbauer spectroscopy (CEMS), x-ray absorption spectroscopy (XAS), and transmission electron microscopy (TEM). Sn ion implantation was performed at 80 keV with a fluence of 1×10^{16} cm^{-2}, positioning the peak of the implantation profile in the middle of the SiO_2. The annealing treatments were performed in the temperature range 800–1100 °C by rapid thermal processing. CEMS and XAS provided unique information on the local atomic and electronic environment of Sn in SiO_2 allowing a detailed investigation of the effect of different annealing conditions. In the as-implanted state all Sn ions are oxidized (with both Sn^{2+} and Sn^{4+} oxidation states present), while annealing induces the formation of β-Sn nanoclusters. TEM showed that cluster sizes are in the range 7–17 nm. For clusters with average diameter <10 nm, XAS detected a reduction in coordination number and interatomic distances. Both XAS and CEMS indicate an increase in the static disorder in the metallic clusters. The investigated annealing treatments do not lead to a complete precipitation of Sn atoms in the metallic phase, leaving a fraction of them oxidized.

DOI: 10.1103/PhysRevB.68.205419 PACS number(s): 61.46.+w, 61.10.Ht, 61.18.Fs, 61.72.Ww

I. INTRODUCTION

Metallic and semiconducting nanocrystals embedded in dielectric materials are attracting great interest due to their novel electrical and optical properties. In fact, single-electron effects,[1,2] new luminescence properties, and large optical nonlinearities have been reported.[3] Moreover, memory devices using nanocrystals as charge storage elements, light-emitting diodes, and single-electron transistors based on metallic or semiconducting nanoparticles have been demonstrated.[4–7] Sn nanocrystals formed in SiO_2 by ion implantation are studied for their optical and electrical properties. Takeda *et al.* demonstrated that microcrystallite glasses doped by Sn^+ ion implantation show nonlinear optical properties.[8] Recently, the low-energy ion-beam synthesis of Sn nanoclusters in SiO_2 layers has been demonstrated and single-electron effects have been observed at low temperatures.[9,10] In addition, the application of Sn nanoclusters as charge storage elements in memory devices has been proposed. The advantages of using metal nanocrystals instead of the semiconductor ones, for memory applications, are the higher density of states around the Fermi level, a more uniform charging characteristics, and a higher degree of scalability of the system.[11,12]

In this work Sn nanoclusters were synthesized in thin SiO_2 films (<100 nm) by ion implantation followed by different thermal treatments. This method, which is compatible with present silicon technology, may allow the control of size, density, and depth distribution of nanocrystals by varying implantation energy, implantation fluence, and annealing conditions. Ion implantation is used to create a supersaturated solid solution of the implanted species in the near-surface region of the matrix. Annealing is then used both to recover the implantation damage and to obtain a thermally activated and controlled redistribution of the implanted ions by phase separation. Depending mainly on the mobility and solubility of the impurity atoms, precipitation occurs either during the implantation stage or during a subsequent annealing step. The ion implantation process and the following thermal treatments involve different physical and chemical processes, such as the diffusion of the implanted species, and the precipitation and chemical reactions between the constituents of the matrix and the species diffusing from the annealing atmosphere. A deep physical understanding of the precipitate formation and growth in ion implanted materials is a prerequisite for an appropriate control of the nanocrystal fabrication.

Conversion electron Mössbauer spectroscopy (CEMS) is a very powerful tool to investigate the structural and dynamical properties of a solid at the atomic scale. Combined measurements of the hyperfine interactions and of the recoil-free fraction provide information, often not attainable by other methods, on the local symmetry, chemical bonding, and dynamical properties of the probing nucleus. The measured parameters are the isomer shift δ (which is sensitive to the valence states, bond angles, and atomic interdistances), the quadrupole splitting Δ which depends on the symmetry of the charges surrounding the probe nucleus, the fractional

spectral intensity F, and the recoil-free fraction f. The recoil-free fraction f, (Ref. 13) is given by

$$f = e^{-k^2\langle x^2\rangle}, \tag{1}$$

where k is the incident γ-ray wave vector and $\langle x^2\rangle$ the average square displacement of the emitting or absorbing nucleus.

X-ray-absorption spectroscopy (XAS) with synchrotron radiation is also a very powerful tool for the study of the local structure of condensed matter. It is of particular use for the investigation of nanometer-sized clusters since, due to the local nature of the fine-structure effect, the variation of the local structure of a cluster can be easily followed from the dimer molecule to the formation of an extended periodic solid.[14–16] Using XAS, size-dependent changes in the coordination numbers, in the bond lengths, and in the Debye-Waller factor have been detected and studied.[17–21] Moreover, and for the same reasons, XAS is well suited to probe the local structure of implanted atoms.[22,23] By analyzing the x-ray appearance near-edge structure (XANES) and the extended x-ray-absorption fine structure (EXAFS) of the absorption coefficient it is possible to determine whether the implanted atoms are dispersed in the matrix or whether they aggregate to form clusters, and to follow changes as a function of implantation and annealing conditions. Analysis of the EXAFS yields a quantitative determination in the first few coordination shells of the coordination number (CN), the mean interatomic distance R, and the mean-square relative displacement σ_{ij}^2 (MSRD, also known as the EXAFS Debye-Waller factor). For a single-scattering contribution to the EXAFS signal involving atoms i and j, the latter quantity[24,25] is

$$\sigma_{ij}^2 = \langle[(\vec{u}_i - \vec{u}_j)\cdot\hat{r}_{ij}]^2\rangle, \tag{2}$$

where $\langle\rangle$ denotes a configurational average, $\vec{u}_i$ is the instantaneous displacement of atom i from its equilibrium position, and $\hat{r}_{ij}$ is the unit vector joining the equilibrium positions of atoms i and j. We note that f and σ^2 are related quantities, but the former depends only on the average displacement of the single resonating nucleus while the latter depends on the relative displacement of two atoms; moreover, increased thermal or static disorder leads to opposite variations in f and σ^2 (the first decreases, the second increases).

In this paper a combined use of the peculiarities of both XAS and CEMS is made in order to provide a rather complete picture of the local atomic environment of Sn atoms in thin SiO_2 films, either after ion implantation or as a function of different annealing treatments. Additional structural information is obtained by Rutherford backscattering spectrometry (RBS), cross-sectional transmission electron microscopy (XTEM), and high-resolution TEM (HREM).

II. EXPERIMENTAL METHODS

SiO_2 films, 85 nm thick, thermally grown on 3″ (100) p-type silicon substrates, were implanted at room temperature by 80 keV/1×10^{16} cm^{-2} $^{119}Sn^+$ ions for CEMS investigations. The mass separator of the implanter was set to a mass 119 amu, but due to the low relative abundance of ^{119}Sn isotope (8.6%) in the ion source and the limited mass resolution, an isotopically pure beam cannot be achieved and contributions of the neighboring isotopes ^{118}Sn and ^{120}Sn are present. Therefore the final relative abundance of ^{119}Sn in the samples was determined by time-of-flight secondary ion mass spectrometry and found to be equal to 80% of the nominal fluence. The implantation area was 1 cm^2 for all samples. For XAS measurements a second set of samples was prepared in the same conditions by implanting 1×10^{16} cm^{-2} Sn^+ ions with a natural abundance of the different isotopes. The implantation parameters were determined by TRIM simulation.[26] The Sn peak position of the implantation profile was chosen to be in the middle of the SiO_2 layer. Post-implantation annealings were performed in the temperature range 800–1100 °C by rapid thermal processing in a N_2 atmosphere. Table I summarizes the annealing conditions for the samples analyzed by CEMS ($C1$–$C5$) and XAS ($X1$–$X4$).

TABLE I. Analyzed samples: annealing treatments and areal density determined by RBS.

Sample	Thermal treatments (N_2)	RBS areal density ($\times10^{15}$ cm^{-2})
CEMS		
$C1$	As implanted	9.7(3)
$C2$	900 °C, 30 s	9.9(3)
$C3$	900 °C, 120 s	9.8(3)
$C4$	900 °C, 600 s	7.8(2)
$C5$	1100 °C, 30 s	7.9(2)
XAS		
$X1$	As implanted	9.7 (3)
$X2$	800 °C, 120 s	9.6(3)
$X3$	900 °C, 30 s	10.0(3)
$X4$	900 °C, 120 s	10.0(3)

The CEMS measurements have been performed at room temperature using a 15 mCi ^{119m}Sn source in a $CaSnO_3$ matrix which was moved by a standard constant acceleration drive. The samples were incorporated as electrodes in a parallel-plate avalanche detector.[27] The isomer shifts are given relative to $CaSnO_3$. ^{119}Sn CEMS with this detector type is characterized by a high efficiency for the detection of conversion and Auger electrons emitted after the nuclear resonance absorption of the 24-keV Mössbauer γ radiation by the ^{119}Sn nuclei in the samples. The integrated sensitivity to a depth of ≈1 μm is determined by the range of the conversion electrons in the samples.

XAS measurements were performed at the GILDA (BM8) beamline of the European Synchrotron Radiation Facility in Grenoble, France. The Sn absorption coefficient was monitored in the fluorescence mode by using a sagitally focusing Si(311) monochromator[28] and a 13-element hyperpure Ge detector with fast digital electronics, using a peaking time equal to 1 μs. The XAS measurements on these samples are particularly challenging due to the low concentration of the

Sn atoms (with respect to the XAS detection limit) and to the fact that they are embedded in a SiO_2 matrix on a silicon substrate. The low concentration causes a weak signal while the low atomic number of matrix and substrate gives rise to strong Compton scattering, which results in an unwanted background when monitoring the fluorescence signal. Typically, the total number of photons reaching each detector element was approximately 10^4 per second while those falling within the region of interest to count the fluorescence intensity was of the order of 10^3 per second. In order to reduce spectral distortions due to the excitation of Bragg peaks in the substrate and to reduce the thermal damping of the signal, samples were mounted on a vibrating and liquid-nitrogen-cooled holder.[29,30] Powder samples of SnO and SnO_2 and a β-Sn foil were measured in the transmission mode as references.

The RBS measurements were performed at the Rossendorf 2 MV Van de Graaff accelerator with 1.2-MeV He^+ ions. The detection angle was 170°. In order to improve the depth resolution a glancing geometry was chosen with angles between the beam and the normal to the sample of 50° or 70°, respectively, corresponding to exit angles of 30° or 10° with respect to the surface.

TEM analyses were performed by using a Philips CM300 microscope (with line resolution of 0.14 nm) operating at 300 keV. The samples were prepared with the standard polishing, dimpling, and ion-milling procedure. Special care was taken during the measurements in order to keep the beam intensity low enough to minimize the e-beam irradiation effects on the specimens. The crystallinity of the clusters was studied by HREM.

III. EXPERIMENTAL RESULTS

A. RBS

RBS was used to study the Sn redistribution during annealing and to measure the retained areal density of Sn. This areal density in the as-implanted samples $X1$ and $C1$ was found to be equal, within the experimental error, with the target value of 1×10^{16} cm^{-2}. This value was not altered after a rapid thermal annealing at 800 °C for 120 s and at 900 °C for 30 s and 120 s. In contrast, a release of about 20% of Sn from the SiO_2 layer was detected after an annealing at 900 °C for 600 s and at 1100 °C for 30 s. The measured areal densities are summarized in Table I.

B. CEMS

The CEMS spectra of the as-implanted sample C1 and of the samples annealed at 900 °C ($C2$,$C3$,$C4$) and 1100 °C ($C5$) are shown in Fig. 1. The spectra were fitted with the least-squares-fitting NORMOS-90 program.[31] The values of the fitting parameters, isomer shift δ, quadrupole interaction Δ, linewidth Γ, fractional spectral intensity F (in %), as well as the value of the resonant effect ϵ are collected in Table II for each sample.

The CEMS spectrum of the as-implanted sample $C1$ could be fitted satisfactorily with three quadrupole doublets, each of them with different hyperfine parameters Δ and δ as shown in Fig. 1. Approximately 80% of the spectral intensity F is due to the components a and b, related to Sn atom in the oxidation state 2+, while the third doublet c is due to Sn atoms in the oxidation state 4+. The two oxidation states are easily distinguishable having different hyperfine parameters. CEMS spectra of the annealed samples were again fitted with these three components a, b, c and with an additional component d, related to β-Sn. In the sample $C2$ the component d

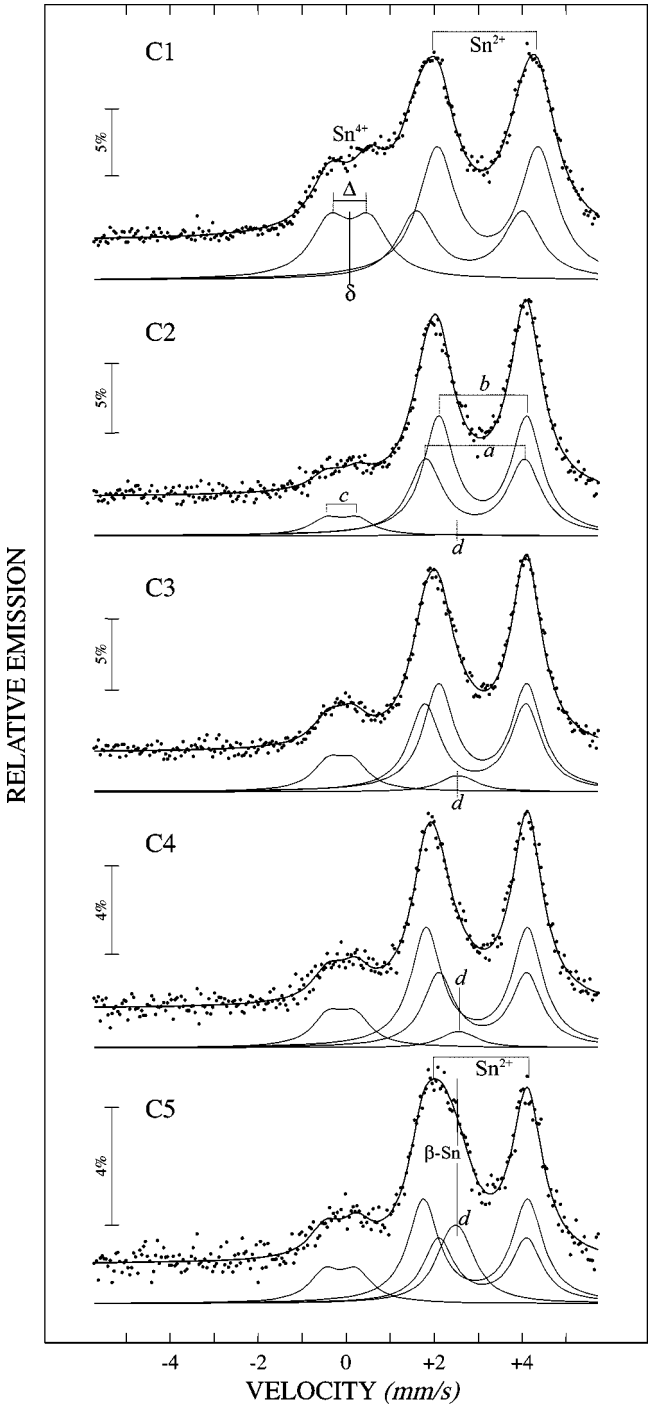

FIG. 1. CEMS spectra of samples $C1-C5$. Dots: experimental data. Continuous thick lines: fit. The spectra were fitted with four components $a-d$, as shown by the CEMS subspectra reported with thin continuous lines.

TABLE II. Hyperfine parameters determined by the fitting of CEMS spectra for componets a–d: isomer shift δ (mm/s), quadrupole interaction Δ (mm/s), linewidth Γ (mm/s), fractional spectral intensity F (in %). Recoil-free fraction $f^*_{\beta\text{-Sn}}$ for the β-Sn phase as determined by our model.

Sample	Parameters	*a* $Sn^{2+}(1)$	*b* $Sn^{2+}(2)$	*c* Sn^{4+}	*d* β-Sn
$C1$	δ	2.80(6)	3.21	0.07(2)	
$\epsilon=0.60(9)$	Δ	2.41(3)	2.30(2)	0.89(3)	
	Γ	1.0(2)	1.04(5)	1.04(5)	
	F	26(10)	52(10)	21.7(8)	
	$f^*_{\beta\text{-Sn}}$				
$C2$	δ	2.93(2)	3.1	−0.10	2.55
$\epsilon=0.41(3)$	Δ	2.25(3)	2.0	0.7	0.3
	Γ	0.92(3)	0.85	0.85	0.85
	F	38(4)	54(4)	7.3(5)	0.5(5)
	$f^*_{\beta\text{-Sn}}$				0.003(3)
$C3$	δ	2.93(1)	3.1	−0.13(3)	2.55
$\epsilon=0.42(3)$	Δ	2.30(2)	2.0	0.55	0.30
	Γ	0.86(3)	0.85	0.85	0.85
	F	38(3)	46(3)	11.5(4)	4.0(6)
	$f^*_{\beta\text{-Sn}}$				0.022(8)
$C4$	δ	2.97(8)	3.1	−0.11(3)	2.55
$\epsilon=0.27(1)$	Δ	2.30	2.0	0.61(6)	0.30
	Γ	0.85	0.85	0.85	0.85
	F	51(3)	32(3)	12.7(6)	4.0(7)
	$f^*_{\beta\text{-Sn}}$				0.022(8)
$C5$	δ	2.93(2)	3.10	−0.12(5)	2.48(2)
$\epsilon=0.22(1)$	Δ	2.37(4)	2.00	0.7	0.30
	Γ	0.85(5)	0.85	1.0(2)	0.85
	F	43(5)	27(5)	12.1(7)	19(1)
	$f^*_{\beta\text{-Sn}}$				0.034(5)

is very weak. The signal in the CEMS spectra related to the electronic configuration Sn^{2+} was fitted consistently for all samples with two distinct components a and b characterized by different quadrupole splittings and isomer shifts. It should be noted that a fitting with only one quadrupole doublet, related to Sn^{2+}, leads to a higher χ-squared and to large values of the linewidth [$\Gamma=1.18(1)$ mm s^{-1}]. The asymmetry observed in samples $C2$-$C3$-$C4$, where the higher-velocity (higher-energy) component in the CEMS spectra is more intense, can be easily explained with the presence of two doublets (a and b) related to the presence of two different Sn^{2+} local configurations. Other effects, such as texture or vibrational anisotropy (Goldanskii-Karyagin effect[32–34]) leading to an asymmetry in the CEMS spectra, would imply the presence of SnO crystallites which, on the basis of the different experimental data, can be excluded (see Sec. IV). As discussed later (Sec. IV A), the observation of two doublets in the SnO-SiO_2 system is quite common and not surprising due to the disordered structure. However, several models have been put forward to explain the nature of the two quadrupole doublets.

Taking into account the fractional spectral intensity F as determined by the fit, the Sn^{2+} phase (components $a+b$) is the predominant one. Moreover, increasing the annealing temperature or the annealing time, the spectral intensity of the component a (with lower δ) increases, while that of the component b (with higher δ) decreases. The β-Sn phase, which is not present in the as-implanted sample, grows after annealing and the related spectral intensity increases with temperature and annealing time.

We observed also a reduction of the resonant effect ϵ in all annealed samples with respect to the as-implanted one. This reduction is more pronounced for the samples $C4$ and $C5$, for which ϵ is about one-third of that observed in sample $C1$. A change of the resonant effect ϵ,

$$\epsilon \propto \sum_i n_{Ai} f_{Ai}, \tag{3}$$

in the different samples is related to a variation of a total number of resonant atoms, and/or to a variation of the relative number of resonant atoms n_{Ai} for each component A_i and/or to a variation of the corresponding recoil-free fraction factors f_{Ai}. Normalizing the experimental CEMS data to the total number of resonant Sn atoms present in the samples and using the known values from the literature for the f_{Ai} factors at 300 K ($f_{\beta\text{-Sn}}=0.04$, $f_{Sn^{2+}}=0.2$, $f_{Sn^{4+}}=0.5$),[13,35,36] it was not possible to explain consistently the decrease in the resonant effect for any of the annealed samples, according to Eq. (3). It should be pointed out that the f values are those known for the bulk compounds, which may be different in our system. In particular, while for Sn^{2+} and Sn^{4+} we used the f values reported in the literature for amorphous compounds in a system similar to ours,[35] in the case of β-Sn we used the value known for the crystalline bulk β-Sn[36] which may be different for nanoparticles.[37]

In order to estimate the $f_{\beta\text{-Sn}}$ factor at 300 K in our samples we made a simple model based on the values of the resonant effects and on RBS results. We assumed also that in our samples the f factor for the oxidized phase are equal to those reported in the literature, while the $f_{\beta\text{-Sn}}$ varies with respect to the bulk value, due to the formation of metallic nanoparticles. RBS measurements showed that in samples $C2$ and $C3$ the measured areal density is constant (Table I). Since the geometrical dimensions of the samples are also the same, we conclude that total number of resonant atoms is the same for the two samples. Taking into account the redistribution of Sn atoms in different components in sample $C3$ with respect to sample $C2$, we calculate $f_{\beta\text{-Sn}}$ (in the following called $f^*_{\beta\text{-Sn}}$) from Eq. (3). We found $f^*_{\beta\text{-Sn}}$ equal to 0.003(3) in sample $C2$ and 0.022(8) in sample $C3$. In samples $C4$ and $C5$, RBS detected a reduction of the total Sn areal density. Therefore for these two samples we normalize the CEMS data to the total number of resonant Sn atoms and we assumed again only a change in the $f_{\beta\text{-Sn}}$ factor. Within experimental error, the ϵ reduction is consistent with a $f^*_{\beta\text{-Sn}}$ for the β-Sn phase of 0.022(8) for sample $C4$ and 0.034(5) for sample $C5$. The obtained values of $f^*_{\beta\text{-Sn}}$ are summarized in Table II. Even if the errors for the values of $f^*_{\beta\text{-Sn}}$ in the different samples are large, it is useful to compare them with the $f_{\beta\text{-Sn}}$ bulk value. This model will be further discussed in connection with XAS and TEM results.

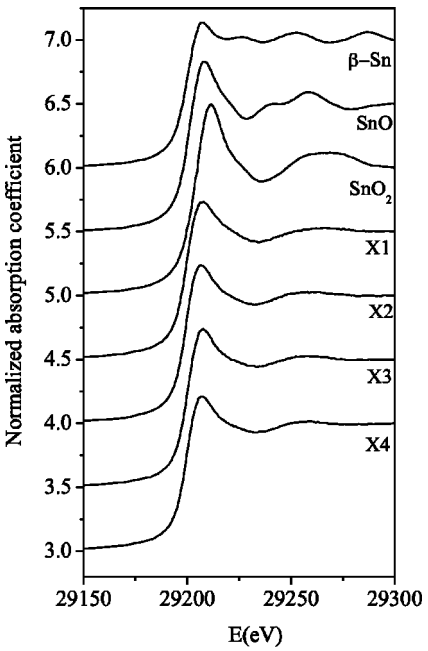

FIG. 2. XANES spectra of Sn implanted SiO_2 films and reference compounds β-Sn, SnO, and SnO_2.

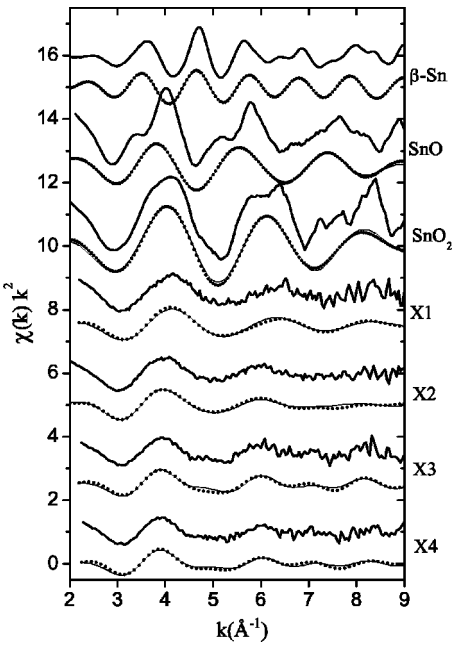

FIG. 3. EXAFS spectra and fit for the reference compounds and the Sn implanted samples $X1-X5$. Continuous thick lines: raw EXAFS data; dot lines: filtered contribution of the first coordination shell; continuous thin lines: fit.

Temperature-dependent measurements are also in progress to determine experimentally the Debye temperature and the real *f* factors for the different phases in our system.

C. XAS

Figure 2 shows XANES spectra for the three standard compounds and the four samples. The pre-edge background was subtracted using a linear fit and the spectra were normalized to 1 at an energy of 29 300 eV. The four samples have a XANES spectrum which exhibits a clear ''white line'' feature typical of oxide compounds and which bears a close similarity to the spectrum of SnO. The absorption edge position (Table III) is close to that of SnO. The major difference of the XANES spectra of the samples with respect to the SnO reference is the absence of the oscillation at approximately 29 240 eV. SnO_2 in which Sn has a 4+ oxidation state, exhibits an absorption edge which is clearly shifted by about 3 eV to higher energies compared to the samples.

To extract EXAFS oscillations, raw absorption data were background subtracted using the AUTOBK routine.[38] Figure 3 shows as the continuous thick lines the raw EXAFS oscil-

TABLE III. Absorption edge position and local strucutural parameters determined by EXAFS: interatomic distances *R*, measured coordination number CN, and mean-square relative displacement σ^2.

Sample	Edge position (eV)	Sn neighbors	*R* (Å)	CN	σ^2 (Å^2)
		Sn_1	3.047(3)	4	0.0060(3)
β-Sn	29200(2)	Sn_2	3.196(4)	2	0.0037(3)
SnO	29201(2)	O	2.230(1)	4	0.001(2)
SnO_2	29204(2)	O_1	1.98(2)	2	0.0(1)
		O_2	2.05(2)	4	0.0(1)
*X*1	29199(2)	O	2.00(1)	2.4(3)	0.008(2)
		O	2.10(3)	2.9(6)	0.020(5)
*X*2	29199(2)	Sn_1	3.0(1)	0.3(5)	0.01(3)
		Sn_2	3.1(1)	0.1(2)	0.01(3)
		O	2.08(2)	1.7(4)	0.004(4)
*X*3	29200(2)	Sn_1	2.96(3)	0.8(4)	0.001(6)
		Sn_2	3.12(3)	0.4(2)	0.001(6)
		O	2.09(4)	2.1(7)	0.018(8)
*X*4	29200(2)	Sn_1	2.94(5)	0.8(7)	0.00(1)
		Sn_2	3.09(3)	0.4(2)	0.00(1)

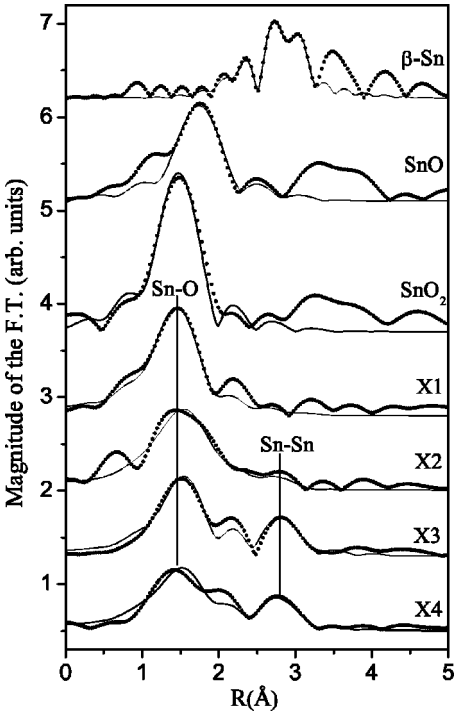

FIG. 4. Magnitude of the FT of the experimental EXAFS data. Dot line: data; continuous lines: fit.

lations for the reference compound and the four Sn implanted samples. The corresponding magnitude of the Fourier transforms (FT) are shown in Fig. 4. All the samples exhibit an EXAFS signal which is typical of a light element backscatterer, such as oxygen; the peak at about 1.5 Å in the FT is related to the bonding of tin and oxygen atoms in the first coordination shell (we indicate these atomic correlations as Sn-O). With increasing annealing temperature and time a higher frequency signal is apparent; this gives rise to a signal at about 2.9 Å in the FT, in good coincidence with the signature of the first shell in β-Sn. This observation indicates that sample annealing gives rise to the formation of Sn-Sn atomic correlations.

EXAFS data were quantitatively analyzed with the FEFFIT programs[38] using theoretical phase signals generated by FEFF 8.0.[39] The analysis was limited to the first coordination shell, due to the limited signal-to-noise ratio of the EXAFS spectra (as explained in the introduction section). Theoretical signals were generated for the Sn EXAFS signal in β-Sn, SnO, and SnO_2, using the known crystallographic structures. These theoretical signals were used in the FEFFIT routine to fit the experimental signals while varying the local structural parameters.

The spectra of the reference compounds were fitted first to test the reliability of the theoretical signals. In this case the CN's were fixed to the known values: for β-Sn the first shell is split in two subshells with CN's equal to 4 and 2, for SnO there is a single subshell with CN's equal to 4 and for SnO_2 there are two subshells, again with CN's equal to 4 and 2. All fits were performed in R space. The β-Sn spectrum was fitted in the range 1.9–3.25 Å using the FT performed in the range 2.5–15 $Å^{-1}$ with a k^2 weight. The oxide spectra were fitted in the ranges 1.3–2.7 Å (for SnO) and 0.35–2 Å (for SnO_2) using the FT obtained in the range 2.5–9 $Å^{-1}$, with the same weight. In all cases the fitting parameters were a common shift of the energy scale, the interatomic distances R, and the mean-square relative displacements σ^2. Figure 3 shows the filtered contribution of the first shell (dot line) along with its fit in k space (thin continuous line), while in Fig. 4 the comparison is performed in R space. The numerical values of the interatomic distances are reported in Table III; in all cases there is good agreement with the known values, with some deviations of the order of at most 0.03 Å for SnO_2, presumably due to systematic errors in background removal, data analysis, and theoretical phase-shift calculation.

The spectra of all the Sn implanted samples were fitted with a combination of a Sn-O signal at a single distance and (except for sample $X1$) of a Sn-Sn signal with a split coordination shell. The spectra were fitted in the ranges 0.25–3.6 Å and 2.5–9.2 $Å^{-1}$. The fitting parameters were the same as the reference compounds with the addition of the CN's for Sn-O and Sn-Sn atomic correlations. The result of the fits is illustrated in Figs. 3 and 4, while in Table III we report the local structural parameters obtained. The error bars correspond to the diagonal elements of the correlation matrix.

We note that the Sn-O interatomic distance is intermediate between those found in SnO and SnO_2, while the Sn-Sn distances are always contracted with respect to the bulk case. In samples $X3$ and $X4$ (annealed at 900 °C), in which the Sn-Sn distances could be determined with a smaller error, the contraction is approximately 0.1 Å. Since Sn is present both in an oxide and in a metallic environment, and since the EXAFS signal is normalized to the total number of atoms (independent of their environment), the experimentally determined CN's are not equal to the real CN's in each of the environments.

We consider a sample in which the excited atoms are present in two phases, with N_α atoms in the phase α and N_β atoms in the phase β; in each phase the excited atoms have a first shell CN equal, respectively, to CN_r^α and CN_r^β . The relation between the measured CN of a given phase (CN^γ with $\gamma=\alpha$ or β) and the real CN_r is (for instance, for the α phase):

$$CN^\alpha = CN_r^\alpha \frac{N_\alpha}{N_\alpha + N_\beta}. \tag{4}$$

In Table III the quantities reported are the measured coordination numbers CN^γ. The measured Sn-O CN is always relatively low compared to the reference crystals and varies between roughly 2 and 3; the total Sn-Sn CN is also low and reaches 1.2(8) in samples $X3$ and $X4$. In order to calculate the real CN_r's it would be necessary to know the relative number of Sn atoms in each environment. This point will be further discussed in the following section where the information obtained from CEMS will be used to address this problem.

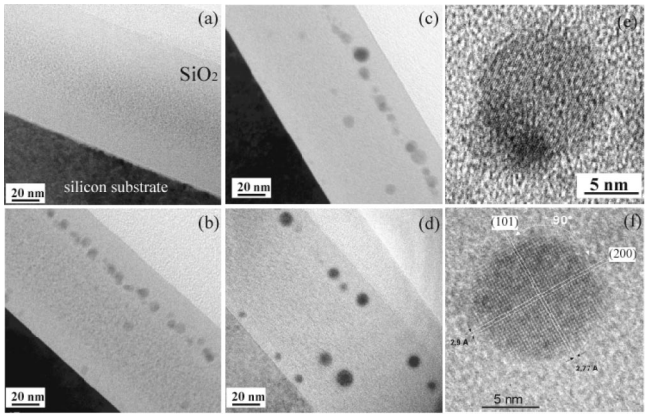

FIG. 5. XTEM images of Sn as-implanted sample (a) and of samples annealed at 800 °C (b) and 900 °C for 30 s (c) and 120 s (d). HREM images of crystalline β-Sn clusters related to the XTEM images of Fig. 6(c) and 6(d) are reported, respectively, in (e) and (f).

D. TEM

Figure 5 shows the XTEM images of the as-implanted sample (a) and of samples annealed at 800 °C for 30 s (b), 900 °C for 30 s (c), and 900 °C for 120 s (d). In the as-implanted sample there is no evidence of metallic nanocrystals. The SiO_2/Si interface is damaged and a contrast close to the middle of the oxide is visible. HREM images on this sample (not shown) revealed the presence of small amorphous clusters with diameters 1.5–2.5 nm.

After annealing at 800 °C [Fig. 5(b)], an additional layer of amorphous cluster (3–6 nm diameter) is formed close to the surface. The contrast in the middle of the oxide in the TEM image is still present and related to a large concentration of Sn atoms, also agglomerated in small amorphous clusters (<2 nm diameter).

After annealing at 900 °C [Figs. 5(c) and 5(d)], the size and number of the clusters increase with annealing time. Even if most of the clusters are still found close to the SiO_2 surface, some clusters grow at the center of the oxide and at the SiO_2/Si interface (as confirmed by XTEM images in different points of the sample).

Figure 6 shows the XTEM image of sample *C*5 annealed at 1100 °C for 30 s, where a large number of metallic Sn clusters were formed in the SiO_2 layer. Moreover, the bigger clusters in all samples annealed at 900 °C and 1100 °C were found to be crystalline. Most of the crystalline clusters imaged by HREM [Figs. 5(e) and 5(f)] show distances between the crystal planes of 2.9 Å. This value may be consistent with both β-Sn and SnO. However, it was also possible to image, in the same nanocrystal, crossing planes which allow an unambiguous identification with β-Sn. For instance, Fig. 5(f) shows the HREM image of a nanocrystal in sample *X*4. The (200) (lattice spacing of 2.9 Å) and the (101) (lattice spacing of 2.77 Å) crossing planes with an angle of 90° between them identify a β-Sn nanocrystal. With increasing annealing time or temperature the mean diameter of the nanocrystals increases from 7.4(6) nm (900 °C, 30 s) to 10.9(9) nm (900 °C, 120 s), 15.2(4) nm (900 °C, 600 s), and 16.9(7) nm (1100 °C, 30 s).

IV. DISCUSSION

A. Oxidized phase

In the as-implanted sample both CEMS and XAS revealed the presence of Sn atoms only in an oxidized state, in agreement with TEM analyses [Fig. 5(a)]. Only after annealing there is a precipitation of a fraction of Sn atoms in a metallic phase.

The predominant valence state of the oxidized phase was determined for all samples by CEMS as Sn^{2+} (component $a+b$) and attributed to SnO, while the smaller fraction in the Sn^{4+} form attributed to SnO_2. The position of the edge and the overall line shape of the XANES spectra reported in Fig. 2 for the as-implanted and the annealed samples show that the predominant oxidation state of Sn atoms is 2+ in agreement with CEMS. However, the absence of the oscillation at approximately 29 240 eV, evident in the XANES spectrum of the SnO crystalline reference compound, suggests that the local structure is not that of the ordered SnO crystal, but is considerably more disordered. Both XAS and CEMS revealed a major disorder in the as-implanted samples, most likely related to the ion implantation damage in the SiO_2 films. Moreover, our results show that also after annealing the local environment of the Sn atoms in the oxidized phase is still different from that of a bulk SnO compound.

The quantitative analysis of XAS showed that in the as-implanted sample the Sn-O bond length is highly contracted and the CN is reduced relative to the reference compound SnO (Table III). After annealing, XAS revealed a variation of the Sn local atomic environment. The Sn-O bond lengths increase, but are still contracted with respect to the bulk values; the CN's are still low. This shows that Sn atoms in the oxidized phase are probably in nonstoichiometric coordination. Our quantitative data on the Sn-O correlations (Table III) can be usefully compared to a recent report on the local structure of bulk tin silicate glasses obtained by neutron diffraction.[40] The authors showed that in tin silicate glasses Sn is a network former and it is present mainly in a $[SnO_3]$ triangular pyramid coordination, while a smaller amount is in a four-oxygen coordination in square pyramid $[SnO_4]$. Both configurations are related to Sn^{2+}. It was also shown that a correlation exists between the Sn-O CN and the Sn-O interatomic distances, which were reported in the range 2.12–2.13 Å for Sn-O CN's of approximately 3. The bond length decreases to around 2.0 Å for CN of 2. The local structural parameters determined by XAS in the as-implanted sample [Sn-O interatomic distance of 2.00 Å and the CN of 2.4(3)] are compatible with the cited correlation between CN and interatomic distance. Upon annealing the Sn-O interatomic distance increases to 2.08–2.10 Å. According to Bent *et al.*,[40] this distance indicates a CN of 3, in agrement with our results.

The signal related to Sn^{2+} in the CEMS spectra was fitted with two distinct components *a* and *b*, suggesting that Sn atoms with valence state 2+ are present in two different local environments. The hyperfine parameters δ and Δ found for both components in the as-implanted and annealed samples are greater than those reported for bulk crystalline and amorphous SnO.[41] Collins *et al.*[41] observed that δ and Δ

values increase in amorphous SnO with respect to the crystalline compound and they suggested that the local environment of amorphous Sn^{2+} can be described by a distorted cell. Our δ and Δ values are even larger than those reported by Collins *et al.* and closer to those found in float glass,[42] binary oxides SnO-SiO_2,[43] and ion implanted glasses.[44] The isomer shift is a measure of the electron density at the Mössbauer nuclei and it is approximately linearly related to the number of 5*s* electrons on the tin atoms.[45,46] A larger value of δ is found in compounds with a more covalent bound. The quadrupole splitting Δ is a measure of the distortion of the local environment of the tin atoms from cubic symmetry and the larger value of the Δ of Sn^{2+} may be related to a change in the structure, e.g., the O-Sn-O angles or bond length, which decrease the point symmetry at the tin atoms. The CEMS results obtained in this work can be also compared with the work of Williams *et al.*[43] who studied the SnO-SiO_2 system with different tin concentration (from 17 to 70 SnO mol % in SiO_2) and found that both Δ and δ increase with decreasing tin content. The large values of the Mössbauer parameters determined in our work are consistent with the trend observed by Williams and co-workers, taking into account the low SnO molar concentration in our samples ($<1\%$). In addition, under specific annealing conditions, these authors observed the presence of two distinct components with different quadrupole splittings and isomer shifts for Sn^{2+}. They suggested that one of these components (δ:2.8 mm/s and Δ:1.2–1.5 mm/s) could be related to crystalline SnO, while the other one (δ: 2.87–3.06 mm/s and Δ: 2.15–2.58 mm/s) to Sn^{2+} present in the $SnSiO_3$ compound or remaining in the glass phase.

In the following we will discuss more in detail the evolution of the oxidized phase with annealing treatments. CEMS showed that annealing leads to a decrease of the total spectral intensity related to the oxidized phase, due to the growth of the β-Sn phase. In particular, CEMS revealed a decrease of the spectral intensity related to components *b* (Sn^{2+}) and *c* (Sn^{4+}); while the spectral intensity of component *a* (Sn^{2+}) increases with respect to the as-implanted state. Compared to the as-implanted samples, the value of Δ decreases for both components *a* and *b*, indicating a rearrangement of the local structure leading to a more symmetrical environment around the Sn atoms. The spectral intensity of the component *a* increases after annealing and the isomer shift is closer to that of amorphous SnO. This component can be related to the presence of small amorphous SnO_x clusters. The hyphothesis is based on TEM results, which revealed the presence of amorphous small clusters (2–3 nm) together with bigger ones associated with β-Sn. The formation of small oxide clusters in Sn ion implanted oxides has been also reported in the literature.[47] The component *b* can be associated to Sn dissolved in the matrix. Its spectral intensity decreases with annealing indicating that a fraction of these atoms precipitates into β-Sn nanoclusters, as confirmed also by XAS and TEM.

Finally, the presence of a large amount of Sn atoms still remaining dissolved in the matrix even after annealing may be due to the high solubility of the SnO oxide in SiO_2. The SnO-SiO_2 system has been studied by different authors,[40,48] showing that SnO may be incorporated into SiO_2 up to a concentration of 60–70 wt %. The behavior of the SnO-SnO_2 system with temperature is not fully understood; different chemical reactions may occur, such as the decomposition of SnO into SnO_2 and β-Sn and the formation of the metastable compound $SnSiO_3$ which in turn decomposes at temperature higher than 700 °C into SnO_2, β-Sn, and SiO_2. The Sn implantation in thin SiO_2 films leads to a system not fully comparable with the SnO-SiO_2 system reported in the literature. Ion implantation forms a highly inhomogeneous Sn distribution in the oxide (Gaussian distribution) and the in diffusion of moisture from the annealing ambient may have a strong influence on these thin SiO_2 films.[49] Nevertheless, our results indicate that the behavior of Sn implanted in silicon dioxide films during annealing may be described to a certain extent taking into account the chemical reactions cited above.

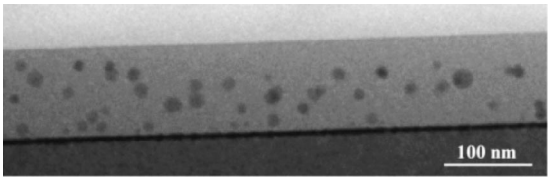

FIG. 6. XTEM image of sample *C*5.

B. Metallic phase

After annealing at 900 °C and 1100 °C, XAS and CEMS spectra showed the formation of the metallic β-Sn phase. However, a certain fraction of Sn atoms still remains coordinated with oxygen. We associate the metallic phase with the formation of β-Sn nanocrystals, as shown also by XTEM and HREM analyses (Figs. 5 and 6). After the annealing at 800 °C for 30 s (sample *X*2), XAS showed that most of the Sn atoms are still predominantly coordinated with oxygen, even if the presence of Sn-Sn correlations cannot be definitely ruled out. In the same sample TEM images revealed the presence of few amorphous nanoclusters with diameters 3–6 nm [Fig. 5(b)] and from TEM it is not possible to conclude if they are metallic or not.

Quantitative determination of the interatomic distance by XAS showed a contraction of approximately 0.1 Å in the metallic Sn nanoclusters, the dimensions of which are known from TEM to be less than 10 nm. The contraction of the lattice parameter has been already observed in small particles and can be ascribed to the hydrostatic pressure due to the cluster surface stress and to that exerted by the matrix. By using the EXAFS technique, lattice contractions in particles of dimensions below 5 nm of various elements such as Au,[21] Ag,[14,16] Cu,[15,20] and rare gases[17–19] have been reported. The value of the hydrostatic pressure acting on the particle can be derived from the lattice-parameter contraction; 26–58 kbars are reported for nanometric sized Cu clusters in amorphous silica,[20] 5–35 kbars for Xe clusters in crystalline Si,[18] and 24–44 kbars for Ar clusters in crystalline Si and Al.[17] Knowing the bulk modulus of Sn ($B_{Sn}=580$ kbars) and supposing an isotropic strain of the particle (i.e., $\Delta a/a=\Delta b/b=\Delta c/c$) we found pressures of 42 ± 16 kbars and 57

± 9 kbars, respectively for the 900 °C 30 s and 900 °C, 120 s samples. These values are similar to the ones reported in the quoted literature for other cluster systems. The rather high value of the contraction in the bond lengths (≈ 0.1 Å) is therefore compatible with a reasonable value of the pressure inside the cluster and this provides *a posteriori* support for our experimental finding.

The Sn-Sn CN determined from XAS quantitative analysis is rather small (Table III). Since the XAS signal is normalized to the total number of Sn atoms, we should calculate the real CN_r for the Sn-Sn and Sn-O correlations using Eq. (4). To do this, we first calculate from CEMS data the percentage of Sn atoms in the metallic (component *d*) and oxide environments (components *a*, *b*, *c*) using the *f* values reported in the literature for the oxidized phase and the $f^*_{\beta\text{-Sn}}$ values determined by our model for the metallic nanoparticles, as explained in Sec. III B. Therefore, from Eq. (4), we calculate that the real CN_r for the metallic phase in samples $X3$ and $X4$ is around 5. This value is slightly lower than the one for bulk β-Sn (CN=6), and qualitatively compatible with the quoted reduction of coordination number observed in nanoclusters. Moreover, the CN number for the Sn-O correlation in annealed samples (as determined with the hypothesis $f_{\beta\text{-Sn}}=f^*_{\beta\text{-Sn}}$) is found to be close to 3; the same value obtained for the samples $X1$ and $X2$ where the Sn-Sn correlations are not present. It should be pointed out that unrealistic values for the CN's of the metallic phase were obtained if the value f_{bulk} for the β-Sn phase was used. These results support the hypothesis of a reduction, in our samples, of the *f* value (at 300 K) for β-Sn nanoparticles with respect to the bulk, as discussed in Sec. III B.

Finally, taking into account the TEM results, we found that there is a trend on the variation of $f^*_{\beta\text{-Sn}}$ with the nanocrystal size (Fig. 7). $f^*_{\beta\text{-Sn}}$ is remarkably lower for the clusters with dimension <10 nm with respect to the value of the crystalline compound. Our results can be compared with those reported by Koops *et al.*,[37] indicating a significant reduction of the recoil-free fraction for metallic β-Sn nanoclusters in SiO_2. An increase in the MSRD has been previously reported by XAS in Au nanoclusters,[50] the origin of which was shown to be precisely a modification of the vibrational structure of the clusters. The determination of the MSRD in the present case unfortunately suffers from an error bar which is too high to be of any real use. Clearly, a more thorough understanding of this issue would require a detailed and temperature-dependent comparison of *f* and MSRD.

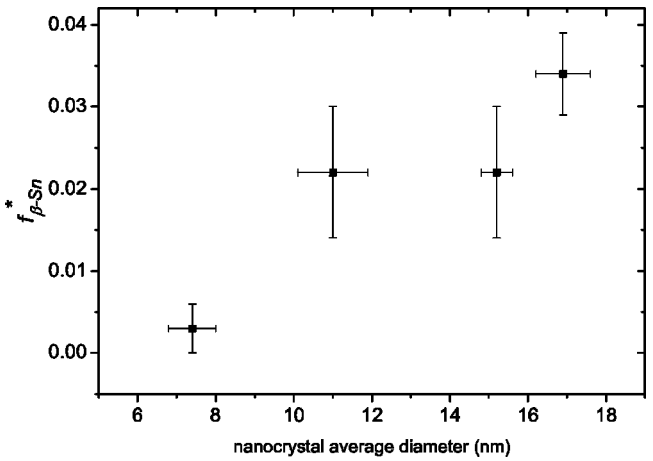

FIG. 7. Recoil-free fraction $f^*_{\beta\text{-Sn}}$ vs nanocrystal size.

V. CONCLUSIONS

CEMS and XAS measurements provided otherwise unavailable information on the evolution of the local environment, as a function of thermal treatments, of Sn atoms implanted in thin SiO_2 films. Both techniques showed that Sn atoms are present only in the oxidized phase in the as-implanted samples. The predominant oxidation state was identified as Sn^{2+}. The thermal treatments lead to the precipitation of a fraction of Sn^{2+} atoms into β-Sn nanoaggregates. Sn atoms remain predominantly coordinated with oxygen for thermal treatments at 800 °C or 900 °C, while the Sn-Sn metallic coordination is predominant after annealing at 1100 °C. The β-Sn phase, observed by CEMS and XAS, is related to Sn crystalline clusters, in agreement with TEM analyses. XAS data show a reduced CN and a contraction of the interatomic distance of approximately 0.1 Å for cluster size below 10 nm. Preliminary CEMS results indicate a reduction of the recoil-free fraction for the β-Sn nanocrystals with respect the known value for the bulk. The percentage of Sn atoms remaining coordinated with oxygen after annealing is due to atoms dissolved in the matrix (as SnO oxide with a distorted cell) or in small precipitates of SnO_x.

ACKNOWLEDGMENTS

The Sn ion implantation has been performed at the Institute of Ion Beam Physics and Materials Research of the Research Center Rossendorf, Dresden (Germany) in the framework of the ''Access to Research Infrastructures'' project funded by the European Community. Measurements at ESRF, Grenoble (France) were supported by the INFM-Commissione Luce di Sincrotrone.

[1] Y. Inoue, A. Tanaka, M. Fujii, S. Hayashi, and K. Yamamoto, J. Appl. Phys. **86**, 3199 (1999).
[2] W. Chen, H. Ahmed, and K. Nakazoto, Appl. Phys. Lett. **66**, 3383 (1995).
[3] S. Okamoto, Y. Kanemitsu, K.S. Min, and H.A. Atwater, Appl. Phys. Lett. **73**, 1829 (1998).
[4] S. Tiwari, F. Rana, H. Hanafi, A. Hartstein, E. Crabbe, and K. Chan, Appl. Phys. Lett. **68**, 1377 (1996).
[5] N. Lalic and J. Linnros, J. Lumin. **80**, 263 (1999).
[6] W. Chen and H. Ahmed, J. Vac. Sci. Technol. B **15**, 1402 (1997).
[7] E. Kapetanakis, P. Normand, D. Tsoukalas, K. Beltsios, J. Stoemenos, S. Zhang, and J. Van den Berg, Appl. Phys. Lett. **77**,

3450 (2000).
[8] Y. Takeda, T. Hioki, T. Motohito, S. Noda, and T. Kurauchi, Nucl. Instrum. Methods Phys. Res. B **91**, 515 (1994).
[9] A. Nakajima, T. Futatsugi, N. Horiguchi, and N. Yokoyama, Appl. Phys. Lett. **71**, 3652 (1997).
[10] A. Nakajima, T. Futatsugi, H. Nakao, T. Usuki, N. Horiguchi, and N. Yokoyama, J. Appl. Phys. **84**, 1316 (1998).
[11] Z. Liu, C. Lee, V. Narayanan, G. Pei, and E.C. Kan, IEEE Trans. Electron Devices **49**, 1606 (2002).
[12] Z. Liu, C. Lee, V. Narayanan, G. Pei, and E.C. Kan, IEEE Trans. Electron Devices **49**, 1614 (2002).
[13] A. Barla, R. Rüffer, A.I. Chumakov, and J. Metge, Phys. Rev. B **61**, R14 881 (2000).
[14] P.A. Montano, W. Schulze, B. Tesche, G.K. Shenoy, and T.I. Morrison, Phys. Rev. B **30**, 672 (1984).
[15] P.A. Montano, G.K. Shenoy, E.E. Alp, W. Schulze, and J. Urban, Phys. Rev. Lett. **56**, 2076 (1986).
[16] P. Lagarde, S. Colonna, A.M. Flank, and J. Jupille, Surf. Sci. **524**, 102 (2003).
[17] G. Faraci, S. La Rosa, A.R. Pennisi, S. Mobilio, and G. Tourillon, Phys. Rev. B **43**, 9962 (1991).
[18] G. Faraci, A.R. Pennisi, A. Terrasi, and S. Mobilio, Phys. Rev. B **38**, 13 468 (1988).
[19] G. Faraci, A.R. Pennisi, and J.L. Hazemann, Phys. Rev. B **56**, 12 553 (1997).
[20] F. d'Acapito, E. Cattaruzza, F. Gonella, S. Mobilio, J.R. Regnard, and F. Spizzo, J. Phys. IV **7**, C2-1107 (1997).
[21] A. Balerna, E. Bernieri, P. Picozzi, A. Reale, S. Santucci, E. Burattini, and S. Mobilio, Phys. Rev. B **31**, 5038 (1985).
[22] F. d'Acapito, S. Mobilio, E. Cattaruzza, F. Gonella, F. Caccavale, P. Mazzoldi, G. Battaglin, and J.R. Regnard, J. Appl. Phys. **87**, 1819 (2000).
[23] S. Spiga, M. Fanciulli, N. Ferretti, F. Boscherini, F. d'Acapito, G. Ciatto, and B. Schmidt, Nucl. Instrum. Methods Phys. Res. B **200**, 171 (2003).
[24] G. Dalba and P. Fornasini, J. Synchrotron Radiat. **4**, 243 (1997).
[25] G. Beni and P. Platzman, Phys. Rev. B **14**, 1514 (1976).
[26] J. F. Ziegler, J. P. Biersack, and U. Littmark, *The Stopping and Range of Ions in Solids* (Pergamon Press, New York, 1996).
[27] G. Weyer, *Applications of Parallel-plate Avalanche Counters in Mössbauer Spectroscopy*, in *Mössbauer Effect Methodology* (Plenum, New York, 1976), p. 301.
[28] S. Pascarelli, F. Boscherini, F. D'Acapito, J. Hrdy, C. Meneghini, and S. Mobilio, J. Synchrotron Radiat. **3**, 147 (1996).
[29] V. Tullio, F. D'Anca, F. Campolungo, F. D'Acapito, F. Boscherini, and S. Mobilio, LNF Report No. LNF-01/020(NT), 2001 (unpublished).
[30] M. Tormen, D. DeSalvator, M. Natali, A. Drigo, F. Romanato, F. Bocherini, and S. Mobilio, J. Appl. Phys. **86**, 2533 (1999).
[31] R. A. Brandt, Wissenschaftliche Elektronik GmBH, Starubey, Germany (1994).
[32] V.I. Goldanskii, E.F. Makarov, and V.V. Khrapov, Phys. Lett. **3**, 334 (1963).
[33] S.V. Karyagin, Dokl. Akad. Nauk SSSR **148**, 1102 (1963).
[34] M.S. Moreno and R.C. Mercader, Phys. Rev. B **50**, 9875 (1994).
[35] K.F.E. Williams, C.E. Johnson, J. Greengrass, B.P. Tilley, D. Gelder, and J.A. Johnson, J. Non-Cryst. Solids **211**, 164 (1997).
[36] M. Yacub and C. Hohenemser, Phys. Rev. **127**, 2028 (1962).
[37] G.E.J. Koops, S. Nauwelaerts, R. Venegas, A. Vantomme, and H. Pattyn, Nucl. Instrum. Methods Phys. Res. B **178**, 93 (2001).
[38] S.I. Zabinsky, J.J. Rehr, A. Ankudinov, R.C. Albers, and M.J. Eller, Phys. Rev. B **52**, 2995 (1995).
[39] A.L. Ankudinov, B. Ravel, J.J. Rehr, and S.D. Conradson, Phys. Rev. B **58**, 7565 (1998).
[40] J.F. Bent, A.C. Hannon, D. Holland, and M.M.A. Karim, J. Non-Cryst. Solids **232–234**, 300 (1998).
[41] G.S. Collins, T. Kachnowski, N. Benczer-Koller, and M. Pasternak, Phys. Rev. B **19**, 1369 (1979).
[42] G. Principi, A. Maddalena, A. Gupta, F. Geotti-Bianchini, S. Hreglich, and M. Verità, Nucl. Instrum. Methods Phys. Res. B **76**, 215 (1993).
[43] K.F.E. Williams, C.E. Johnson, D. Holland, and M.M. Karim, J. Phys.: Condens. Matter **7**, 9485 (1995).
[44] T. Barancira, R. Moons, G.E.J. Koops, W. Deweerd, H. Pattyn, M. Tzenov, D. Dimova-Malinovska, T. Tsvetkova, R. Venegas, and G.L. Zhang, J. Non-Cryst. Solids **244**, 189 (1999).
[45] A. Svan, N.E. Christensen, C.O. Rodrigues, and M. Methfessel, Phys. Rev. B **55**, 12 572 (1997).
[46] P.E. Lippens, Phys. Rev. B **60**, 4576 (1999).
[47] A. Markwitz, R. Grötzschel, K.H. Heinig, L. Rebohle, and W. Skorupa, Nucl. Instrum. Methods Phys. Res. B **76**, 251 (1999).
[48] M.M. Karim and D. Holland, Phys. Chem. Glasses **36**, 206 (1995).
[49] B. Schmidt, D. Grambole, and F. Herrmann, Nucl. Instrum. Methods Phys. Res. B **191**, 482 (2002).
[50] A. Balerna and S. Mobilio, Phys. Rev. B **34**, 2293 (1986).